Broadband Low-Frequency Acoustic Metamuffler

Lang Shen,[1,‡] Yifan Zhu,[2,‡] Feilong Mao,[1] Siyuan Gao,[1] Zihao Su,[1] Zhitao Luo,[1] Hui Zhang,[1,*] and Badreddine Assouar[2,†]

[1] *Jiangsu Key Laboratory for Design and Manufacture of Micro-Nano Biomedical Instruments, School of Mechanical Engineering, Southeast University, Nanjing 211189, China*

[2] *Université de Lorraine, CNRS, Institut Jean Lamour, 54000 Nancy, France*

(Received 12 July 2021; revised 27 October 2021; accepted 10 December 2021; published 23 December 2021)

In this research, we propose and design an acoustic metamuffler (AMM) by coupling a microperforated plate and a composite waveguide formed by a main waveguide and a Helmholtz resonator. The proposed mechanism and deliberately designed structure are conducive to generating multimode resonances that help to improve the coupling absorption effect and lead to broadband (4 octaves) sound insulation. We develop an effective circuit model to analytically predict the insulation bandwidth and put forward numerical and experimental measurements that demonstrate the effectiveness of the proposed concept. The designed AMM produces sound insulation with an average of 20 dB of sound-transmission loss at a low-frequency range, extending from 100 to 1600 Hz, while having an ultrathin thickness of 6.2 cm (1/55λ for the lowest working frequency). Our findings could have pragmatic applications for acoustic insulators or absorbers.

DOI: 10.1103/PhysRevApplied.16.064057

I. INTRODUCTION

In acoustic engineering, it is a key scientific problem to understand how to achieve low-frequency and broadband noise cancellation with small thickness, while maintaining air circulation or ventilation. Traditional sound-absorbing materials and sound barriers not only need huge structural sizes (windows, walls, etc.) to eliminate low-frequency noise, but also cannot guarantee air circulation while eliminating noise [1]. Acoustic metamaterials [2,3] and acoustic metasurfaces [4] can achieve the regulations of low-frequency acoustic waves with subwavelength structural sizes, such as negative refraction, acoustic stealth, and acoustic abnormal reflections [5–7]. Thanks to the great success of acoustic metamaterials and acoustic metasurfaces for low-frequency acoustic wave manipulations, various metastructures have been applied to the design of sound absorbers for application in the noise-control field [8–10]. By employing local resonance and Fano resonance [11–13], sound waves within a certain frequency range can be dissipated and absorbed in the structures, and such designs make it possible for the subwavelength metastructure to regulate low-frequency sound waves; this provides a different strategy for low-frequency acoustic wave manipulations.

Considering that noise is usually broadband, the realization of low-frequency broadband noise cancellation has always been the focus of and challenge for research. The emergence of the coupling structure of multiple resonant modes with optimized structural resonance and acoustic interference provides a different design methodology for broadband sound cancellation [14–17]. Even so, achieving low-frequency and broadband sound cancellation under airflow conditions [11–13,17–20] remains a challenge.

Here, we propose and demonstrate an acoustic metasurface muffler (AMM) to achieve low-frequency wideband noise elimination. In a prior study [21], it was illustrated that tunable acoustic filters could be realized by a composite waveguide consisting of a Helmholtz resonator and the main waveguide. Here, we combine the composite waveguide [21] with a microperforated plate [22–24] as the building block of the AMM to improve the bandwidth of sound insulation. The designed coupled structure helps to increase the resonant mode density of the system [25], especially at very low frequencies. Based on the principle of acoustic absorption interactions and multiparameter resonance units, low-frequency broadband noise elimination is achieved. We first analyze the coupled structure theoretically by developing effective circuit models (acoustic-electric analogy [26]). Then, the effectiveness of the proposed theory is verified through simulation and experiment. Through theory, simulation, and experiment, it is proved that this structure can achieve broadband noise cancellation within the range of 100–1600 Hz (the

*seuzhanghui@seu.edu.cn
†badreddine.assouar@univ-lorraine.fr
‡L. Shen and Y. Zhu contributed equally to this work.

average noise-cancellation amount is higher than 20 dB), and its thickness is only 6.2 cm. The proposed mechanism based on the coupled structure can lead to ultrabroadband (4 octaves) sound insulation, which outperforms previous broadband designs [14–17]. In addition, putting a microperforated panel connected in series introduces an additional trade-off between ventilation performance and sound insulation, since the microperforated plate may block part of the fluid under flowing-fluid-filled circumstances [17]. We therefore evaluate and optimize the ventilation performance in our case. The most critical factor affecting the ventilation performance of the AMM is the ventilation area. Through calculations, it can be concluded that the minimum ventilation area of the AMM designed in this work is about of 81 mm^2, which accounts for about 13% of the cross-section area.

II. RESULTS

A. The coupled silencing structure

As shown in Fig. 1(a), we draw a conceptual diagram of an AMM that consists of a coupled structure connected by a microperforated plate layer and a composite waveguide layer. The structure is a square with a side length of $a = 70$ mm and total thickness of $H = h_1 + h_2 + h_3$. Here, $h_1 = 2$ mm is the thickness of the microperforated plate. $h_2 = 20$ mm is the thickness of the mid-air layer. $h_3 = 40$ mm is the thickness of the composite waveguide layer. The pore diameter of the top microperforated plate is $r = 0.3$ mm, and the perforation rate is $\sigma = \pi r^2/p^2 = 0.4\%$. The outer parameters of the four units (four units) at the bottom are the same. For clarity, the composite waveguide layer is detached to show the details of its inner structure. It has four kinds of composite waveguide units with different parameters. In each unit, the cross-section area of the acoustic main waveguide and the length of the neck are $S_1 = 4 \times 30$ mm^2 and $l = 4$ mm, respectively. The other parameters for the four units are shown in Table I (S_2 is the cross-section area of the necks; V is the volume of the Helmholtz cavity).

TABLE I. Structural parameters of the composite waveguide.

	Unit 1	Unit 2	Unit 3	Unit 4
S_2 (mm^2)	1×1	2×2	3×5	5×7.5
V (mm^3)	18 000	18 000	22 500	22 500

To make the AMM have a broadband muffling effect, each unit has a different sound-absorption and isolation-frequency band. In addition, on the surface of the structure, we also design a microperforated plate structure, the anechoic frequency band of which is just complementary to the composite waveguide layer. As shown in Fig. 1(b), four composite waveguides are conceived explicitly, so that each one has its contribution (highly efficient dissipation or resonance), and they collectively provide remarkable sound blocking over a wide frequency range, while the whole structure features a subwavelength thickness.

B. Theoretical model

The coupled silencing structure is shown in Fig. 1(a). Based on the theoretical analysis, the impedance of the microperforated plate is calculated according to the acoustic-electrical analogy method, and then the acoustic transmission characteristics of the resonant structure are calculated by using the local analysis method, to obtain the sound-transmission loss (STL) of the whole structure. The STL of the coupling structure is determined by

$$L_{ST} = 10 \log_{10} \frac{1}{I_I}, \tag{1}$$

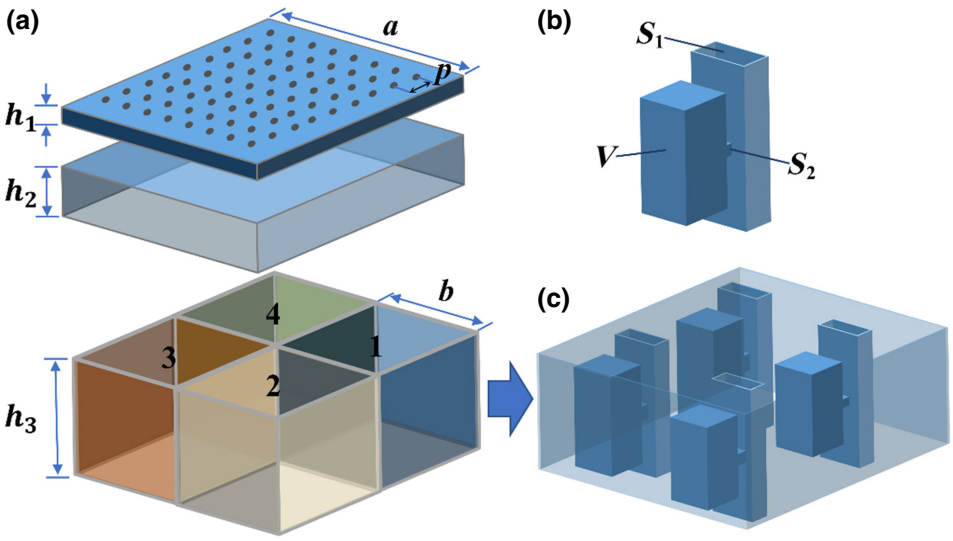

FIG. 1. (a) Schematic diagram of AMM and the unit's composition. (b) Composite waveguide units have a different internal size and are divided into three parts: waveguide, neck, and Helmholtz cavity. (c) Composite waveguide layer is composed of four units.

$$t_I = \frac{4}{4\cos^2(k_2 D) + \left(\frac{Z^2+Z_0^2}{ZZ_0}\right)^2 \sin^2(k_2 D)}, \tag{2}$$

where t_I is the transmission coefficient of sound intensity, $k_2 = 2\pi f/c_0$ is the wave number, D is the width of the structure, f is the frequency of the incident sound wave, $Z = \rho_0 c_0$ is the characteristic impedance of air, Z_0 is the structural impedance, $\rho_0 = 1.21$ kg/m^3, and $c_0 = 343$ m/s represents air density and sound velocity in air.

By using the acoustic-electric analogy, we can calculate the relationship between the acoustic impedance of the structure and the parameters of each structure. It can be seen from Fig. 2(a) that the whole structure satisfies the following conditions:

$$P_0 = P_1 + P_2. \tag{3}$$

The complex impedance of each part is assumed to be Z_1 and Z_2:

$$Z_0 = Z_1 + Z_2. \tag{4}$$

We can determine the magnitude of Z_1 and Z_2 from

$$Z_1 = R_1 + jX_{L1} - jX_{C1}, \tag{5}$$

$$Z_2 = R_2 + jX_{L2} + \frac{R_2R_3 - X_{L2}X_{L3} + X_{L2}X_{C3} + j(R_3X_{L2} + R_2X_{L3} - R_2X_{C3})}{R_2 + R_3 + j(X_{L2} + X_{L3} - X_{C3})}, \tag{6}$$

where the waveguide and microperforation plate can be regarded as an inductor, L, in series with a resistor, R, at low frequencies, Meanwhile, the Helmholtz resonator cavity and cavity backing are equivalent to a capacitor, C. $X_L = 2\pi fL$ and $X_C = 1/2\pi fC$ express inductive and capacitive reactance, respectively. j represents the imaginary unit. Analogous to acoustics and electricity, $L = \rho l/S_2$ and $C = V_0/(\rho_0 c_0^2)$, where V_0 is the volume of the Helmholtz cavity.

For the microperforated plate structure, we can simply calculate its acoustic transmission-loss curve. When the aperture of the microperforated plate is small, its

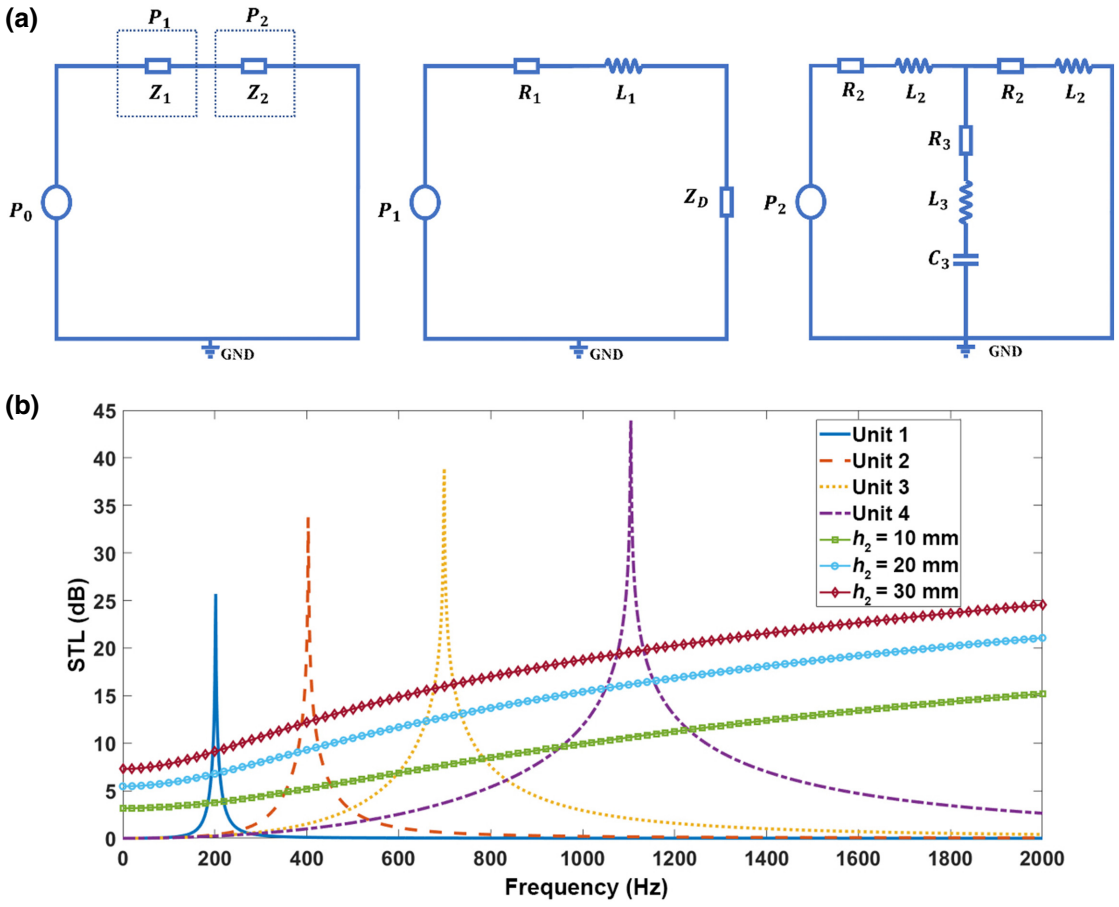

FIG. 2. (a) Acoustic-electrical analogy of acoustic metasurface muffler. Left, acoustic metasurface muffler; middle, microperforated plate; right, composite waveguide. (b) Relationship between transmission loss and frequency for the microperforated plate with different mid-air layer thicknesses (rhombuses, circles, and squares correspond to $h_2 = 10$, 20, and 30 mm, respectively) and different composite waveguides of units 1–4, corresponding to blue, orange, yellow, and purple lines, respectively.

impedance, Z_1, can be expressed as [22]

$$Z_1 \approx \tfrac{4}{3} j\omega\rho t + \tfrac{32\rho\mu t}{d^2}. \quad (7)$$

The acoustic transmission loss of the microperforated plate structure can be calculated by

$$L_{\mathrm{ST}} = -20\ln\left(1 + \tfrac{Z_1\sigma}{2\rho c}\right). \quad (8)$$

The green line in Fig. 2(b) can be obtained by numerical calculations. The results show that the designed microperforated plate structure has a good noise-reduction performance, and the sound-reduction effect is significantly improved within the wider frequency range from 0 to 2000 Hz, theoretically.

For the composite waveguide structure, the acoustic transmission loss can be calculated as follows:

$$t_I = \tfrac{1}{1+(\rho^2c^2)/(4S_2^2X_b^2)}, \quad (9)$$

where $X_b = \omega\rho l/S_2 - \rho c^2/\omega V$. The STL of the composite waveguide structure can be obtained by combining Eq. (9) with Eq. (2). Based on Eqs. (1)–(9), we find that the sound-transmission loss of the AMM highly depends on the parameters of both the microperforated panel and the waveguide. Thus, reasonable structural design parameters can lead to a planar and optimized sound-insulation spectrum, considering the coupling effect between structures.

To further explore the underlying working mechanism, as shown in Fig. 2(a), we establish the acoustic-electric analogy model of the coupled anechoic structure and obtain the changing relationship of the sound-transmission loss of each part of the structure with frequency, according to the acoustic local-analysis method. In Fig. 2(b), here, we focus on the four frequency points of 202, 403, 698, and 1104 Hz, corresponding to units 1–4, respectively, at which the capability of the coupled muffler is dominated by sound absorption induced by viscothermal loss and reflection by effective impedance mismatching. This is due to the resonance of the composite waveguide. As the frequency of the noise increases, the effect of the microperforated plates becomes even more dramatic. According to our design, when the frequency exceeds 1100 Hz, the microperforated plate plays a major role in sound absorption and insulation in the coupling structure.

In brief, the AMM can realize broadband noise elimination because of the existence of the resonance peak for the composite waveguide and the assistance of the microperforated plate. Through the above analysis, it is proved that broadband acoustic suppression comes from the coaction of the four coupled resonant chambers. Empowered by the coupling effect, our muffler has a wide noise-attenuation bandwidth. Compared with the noise-cancellation structure designed solely by interference [27] or dissipation [28] mechanisms, our advantage lies in making full use of the synergistic effect of resonance and dissipation to achieve low-frequency and broadband noise cancellation.

C. Numerical simulation and experimental demonstration

The designed coupled silencing structure is numerically simulated by using the "pressure acoustics, frequency domain" module of COMSOL Multiphysics, in which the frequency domain study is performed to calculate sound transmission through the coupled silencing structure. To be consistent with experimental conditions and estimate its low-frequency behavior under plane-wave incidence, the designed coupled silencing structure is placed within a cylindrical waveguide, both the waveguide wall and coupled silencing structure are considered acoustically rigid in the physical field settings. To avoid the effects of reflected waves, both ends of the waveguide are set as plane-wave radiation boundaries, while the incident wave is a plane wave and the acoustic pressure amplitude is set to 1 Pa. Because there are tiny structures inside, we choose that these regions are "narrow region acoustics" in COMSOL, which can simulate the acoustic structures by considering viscothermal loss.

Figure 3(a) shows the acoustic-pressure-amplitude distributions for different modes (modes 1–5). Incident directions are marked by arrows and the incident pressure is marked by P_i. According to the previous analysis, modes 1–3 (202, 403, and 698 Hz, respectively) are mainly caused by coupling resonance of different composite waveguides, and the additional cavities are formed by microperforated and composite waveguides. In addition, it can be seen from Fig. 3(a) that the composite waveguide structures play a major role in different vibration modes, which are related to our parameter design. For mode 4 (1104 Hz) in Fig. 3, we find that the acoustic pressure amplitude is large not only in the third composite waveguide but also in the mid-air layer. This means that the cavity of the mid-air layer between the microperforated plate and the composite waveguide is also resonant at 1104 Hz. Mode 4 is caused by the coupling resonance of the mid-air layer and the composite waveguide. For mode 5 (1300 Hz) in Fig. 3, we find that the composite waveguide is no longer resonant. Resonance only occurs in the mid-air layer. This is consistent with the theoretical results of the acoustic-electric analogy analysis. Figure 3(b) shows that the improper selection of parameters will reduce the STL of the structure, and the selection of the aperture of the microperforated plate has a great influence on the middle and high frequencies (mode 4 and mode 5). A comparison of the parameters $r = 0.3$ and 0.6 mm shows that $r = 0.3$ mm has higher efficiency, and thus, we choose this optimized radius for the final design. We also plot the curve for the structure with only a microperforated plate in Fig. 3(b) as a reference. The comparison shows that the

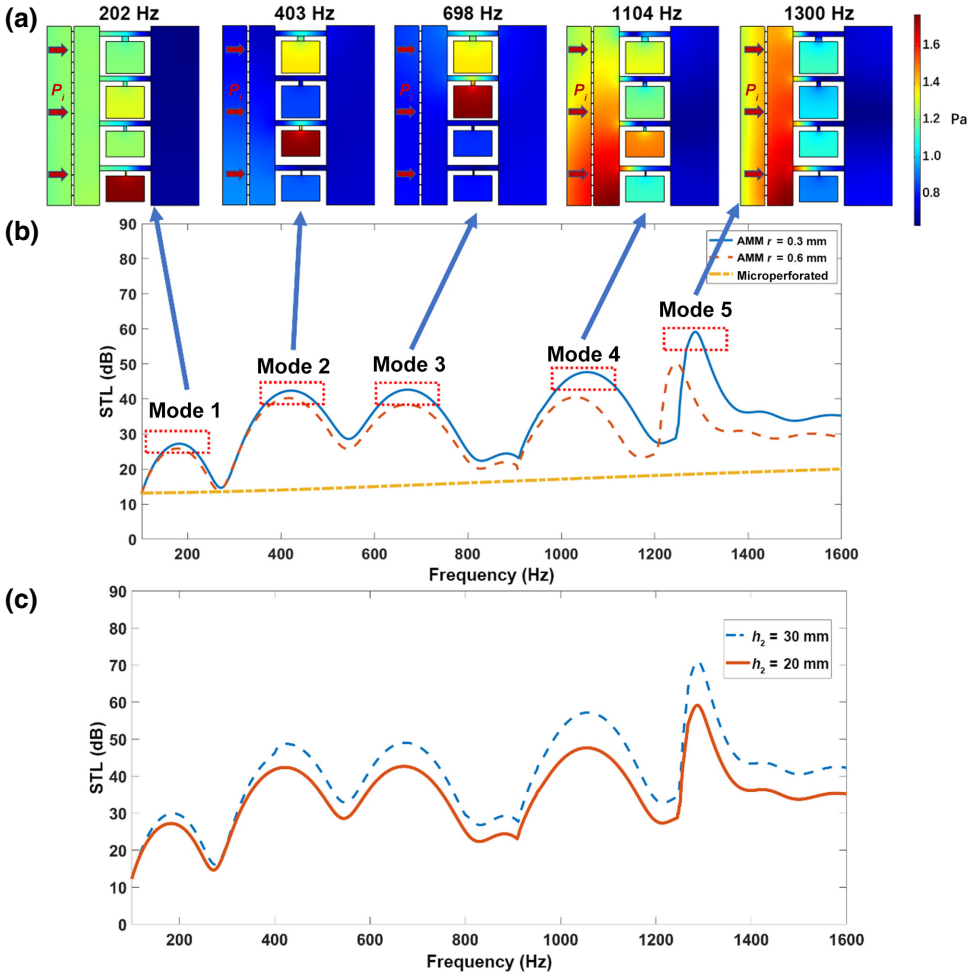

FIG. 3. (a) Sound field distribution in the structure at frequencies of 202, 403, 698, 1104, and 1300 Hz, denoted as modes 1–5, respectively. Incident directions are marked by arrows and incident pressure is marked by P_i. (b) Simulation diagram of the STL curve of the AMM ($r = 0.3$ and 0.6 mm) and microperforated plate ($r = 0.3$ mm). Modes 1–5 are marked in the figure. (c) Simulations considering a mid-air layer with different thicknesses of $h_2 = 20$ and 30 mm.

designed AMM has a higher STL efficiency than that of the microperforated plate. Figure 3(c) shows the simulation considering a mid-air layer with different thicknesses of $h_2 = 30$ and 20 mm. Combining the results in Figs. 3(c) and 2(b), we find that the STL is increasing with the mid-air layer thickness. Considering the trade-off between sample thickness and sound insulation, we choose $h_2 = 20$ mm for sample fabrication.

Meanwhile, the standard impedance-tube system is used for experimental measurements, along with the double-load method [20], where the sample is fixed firmly with clamps in the impedance tube. The experimental setup, consistent with that adopted in numerical modeling, is schematically illustrated in Fig. 4(a). The sample of the AMM, made of photosensitive resin via three-dimensional (3D) printing, is shown in Fig. 4(b). Relevant results are shown in Fig. 4(c). The parameters of the structure are consistent with those used in theoretical calculations.

As can be seen from Fig. 4(c), the theoretical prediction shows excellent agreement with numerical and experimental results, demonstrating the effectiveness of our design. The designed AMM sample blocks more than 90% of incident sound energy in the range of 100−1600 Hz (experimental data). In Fig. 4(c), caused by the resonance of the composite waveguide, there are multiple peaks within 100–1600 Hz. Meanwhile, the dissipation effect of the microperforated plate forces the coupling muffler structure to retain a high muffler capacity. More specifically, harnessing the power of dissipation in combination with resonance remarkably lowers the onset frequency in the current design. It is noted that the "sampled" frequencies do not exactly coincide with the peaks. This is because modes 1–5 are inevitably affected by the coupling resonances between composite waveguides and the mid-air layer. However, we consider that this effect is not obvious in the case of very low sound frequency (modes 1–3), because the resonance frequency for the mid-air layer is between modes 4 and 5.

For the optimization of the frequency band, the design of the fine-distributed composite waveguide is critical in the proposed AMM. In the current study, we theoretically choose 200, 400, 700, and 1100 Hz as four target resonant frequencies, as shown in Fig. 3(b). From mode 5 in Fig. 3, the resonant frequency for the mid-air layer is

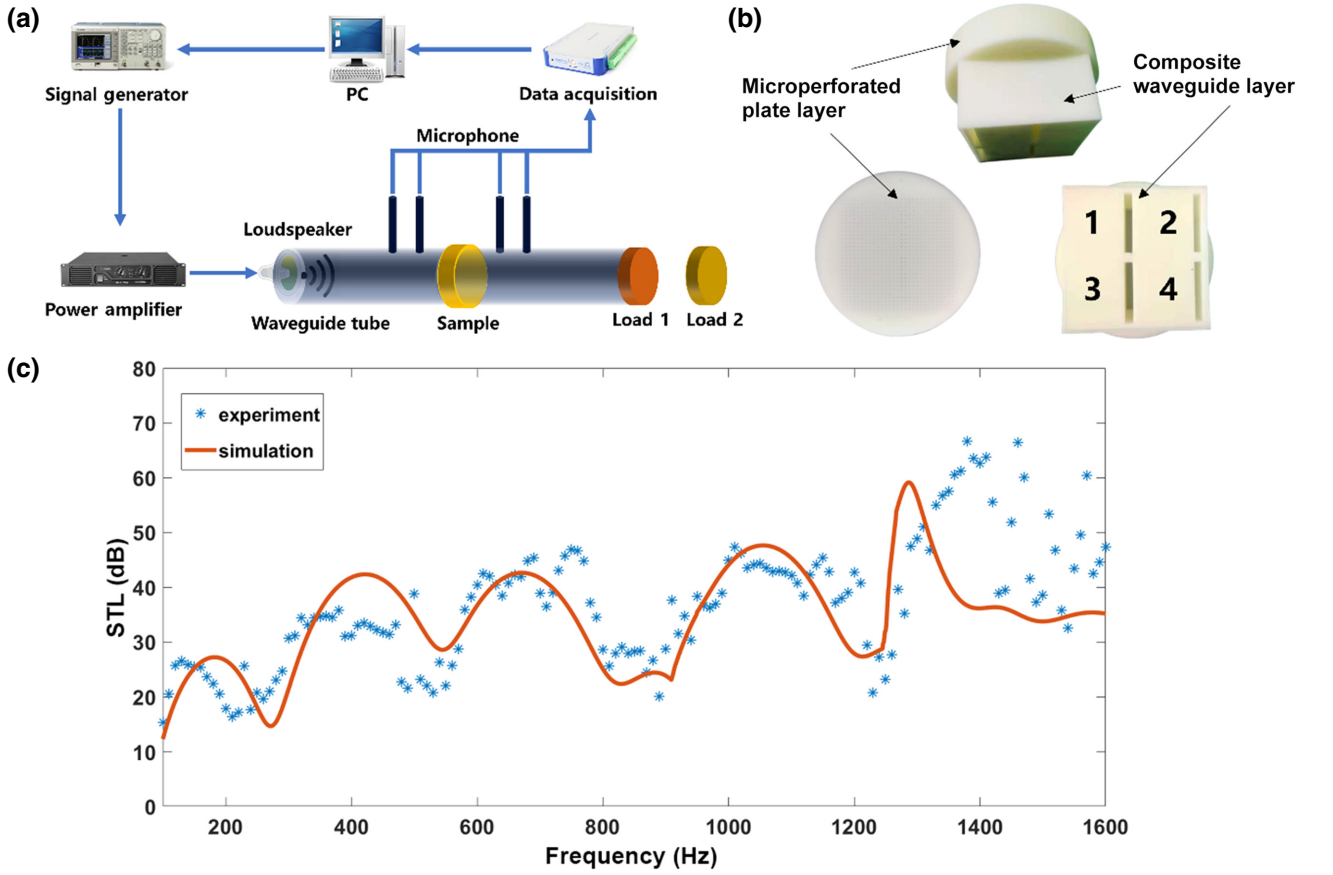

FIG. 4. Diagram of simulation and experiment results. (a) Schematics of the experimental setup for the double-load method, where the specimen is clamped in the impedance tube. (b) 3D-printed sample structure schematic diagram made according to the theoretical model shown in Fig. 1. Numbers 1, 2, 3, and 4 represent different composite waveguide units, which correspond to Fig. 1. (Here, the coupling structure is designed as prescribed by the standard impedance tube for experiments. While following the presented design strategy, it can be straightforwardly reshaped as a cube.) (c) Simulated (red line) and measured (blue asterisk) STL of the designed structure.

1300 Hz. These five frequencies lead to the final broadband absorption spectrum from 100 to 1600 Hz. Different unit cells are deliberately designed to have a continuous bandwidth. The resonant frequency of the composite waveguide is mainly decided by the parameters given in Table I.

III. CONCLUSION

We theoretically and experimentally introduce an analytical model to design an acoustic metamuffler. The acoustic-electrical analogy method is applied to the theoretical analysis, and the FEM results show good agreement with the experimental measurements. We investigate an alternative metastructure composed of a composite waveguide and a microperforated plate. To illustrate the proposed concept and underlying physical mechanism, we combine theory and experiment to achieve a broadband metamuffler operating at a low frequency of 100–1600 Hz, featuring a deep-subwavelength thickness. We show that the designed metastructure helps to enlarge the bandwidth and strengthen the effectiveness of sound insulation in a low-frequency regime.

ACKNOWLEDGMENTS

The authors acknowledge financial support provided by the National Natural Science Foundation of China (Grant No. 11874110).

[1] X. Yu, S.-K. Lau, L. Cheng, and F. Cui, A numerical investigation on the sound insulation of ventilation windows, Appl. Acoust. **117**, 113 (2017).
[2] S. A. Cummer, J. Christensen, and A. Alù, Controlling sound with acoustic metamaterials, Nat. Rev. Mater. **1**, 1 (2016).
[3] G. Ma and P. Sheng, Acoustic metamaterials: From local resonances to broad horizons, Sci. Adv. **2**, e1501595 (2016).
[4] B. Assouar, B. Liang, Y. Wu, Y. Li, and Y. Jing, Acoustic metasurfaces, Nat. Rev. Mater. **3**, 460 (2018).

[5] Y. Li, B. Liang, Z. M. Gu, X. Y. Zou, and J. C. Cheng, Reflected wavefront manipulation based on ultrathin planar acoustic metasurfaces, Sci. Rep. **3**, 2546 (2013).
[6] J. J. Zhao, B. W. Li, Z. N. Chen, and C. W. Qiu, Manipulating acoustic wavefront by inhomogeneous impedance and steerable extraordinary reflection, Sci. Rep. **3**, 2537 (2013).
[7] J. J. Zhao, B. W. Li, Z. N. Chen, and C. W. Qiu, Redirection of sound waves using acoustic metasurface, Appl. Phys. Lett. **103**, 151604 (2013).
[8] Y. Li and B. Assouar, Acoustic metasurface-based perfect absorber with deep subwavelength thickness, Appl. Phys. Lett. **108**, 204301 (2016).
[9] S. Huang, X. Fang, X. Wang, B. Assouar, Q. Cheng, and Y. Li, Acoustic perfect absorbers via spiral metasurfaces with embedded apertures, Appl. Phys. Lett. **113**, 233501 (2018).
[10] K. Donda, Y. Zhu, S. W. Fan, and B. Assouar, Extreme low-frequency ultrathin acoustic absorbing metasurface, Appl. Phys. Lett. **115**, 173506 (2019).
[11] X. Wu, K. Y. Au-Yeung, X. Li, R. C. Roberts, J. Tian, C. Hu, Y. Huang, S. Wang, Z. Yang, and W. Wen, High-efficiency ventilated metamaterial absorber at low frequency, Appl. Phys. Lett. **112**, 103505 (2018).
[12] L. J. Li, B. Zheng, L. M. Zhong, J. Yang, B. Liang, and J. C. Cheng, Broadband compact acoustic absorber with high-efficiency ventilation performance, Appl. Phys. Lett. **113**, 103501 (2018).
[13] R. Ghaffarivardavagh, J. Mikolajczyk, S. Anderson, and X. Zhang, Ultra-open acoustic metamaterial silencer based on fano-like interference, Phys. Rev. B **99**, 024302 (2019).
[14] S. Huang, Z. Zhou, D. Li, T. Liu, X. Wang, J. Zhu, and Y. Li, Compact broadband acoustic sink with coherently coupled weak resonances, Sci. Bull. **65**, 373 (2020).
[15] Y. F. Zhu, K. Donda, S. W. Fan, L. Y. Cao, and B. Assouar, Broadband ultra-thin acoustic metasurface absorber with coiled structure, Appl. Phys. Express **12**, 114002 (2019).
[16] Y. F. Zhu and B. Assouar, Nonlocal acoustic metasurface for ultra-broadband sound absorption, Phys. Rev. B **103**, 064102 (2021).
[17] R. Z. Dong, D. Mao, X. Wang, X. Wang, and Y. Li, Ultra-Broadband Acoustic Ventilation Barriers via Hybrid-Functional Metasurfaces, Phys. Rev. Appl. **15**, 024044 (2021).
[18] H. L. Zhang, Y. F. Zhu, B. Liang, J. Yang, J. Yang, and J. C. Cheng, Omnidirectional ventilated acoustic barrier, Appl. Phys. Lett. **111**, 203502 (2017).
[19] T. Lee, T. Nomura, E. M. Dede, and H. Iizuka, Ultrasparse Acoustic Absorbers Enabling Fluid Flow and Visible-Light Controls, Phys. Rev. Appl. **11**, 024022 (2019).
[20] M. Sun, X. S. Fang, D. X. Mao, X. Wang, and Y. Li, Broadband Acoustic Ventilation Barriers, Phys. Rev. Appl. **13**, 044028 (2020).
[21] H. Zhang, Z. Wei, X. Zhang, L. Fan, J. M. Qu, and S. Y. Zhang, Tunable acoustic filters assisted by coupling vibrations of a flexible helmholtz resonator and a waveguide, Appl. Phys. Lett. **110**, 1315 (2017).
[22] D. Y. Maa, Potential of microperforated panel absorber, J. Acoust. Soc. Am. **104**, 2861 (1998).
[23] X. Yu, L. Cheng, and X. You, Hybrid silencers with microperforated panels and internal partitions, J. Acoust. Soc. Am. **137**, 951 (2015).
[24] J. Kang and M. W. Brocklesby, Feasibility of applying micro-perforated absorbers in acoustic window systems, J. Appl. Acoust. **66**, 669 (2005).
[25] M. Yang, S. Y. Chen, C. X. Fu, and P. Sheng, Optimal sound-absorbing structures, Mater. Horiz. **4**, 673 (2017).
[26] L. Kinsler, *Fundamentals of Acoustics* (Wiley, New York, 1982).
[27] J. Yang, J. S. Lee, H. R. Lee, Y. J. Kang, and Y. Y. Kim, Slow-wave metamaterial open panels for efficient reduction of low-frequency sound transmission, Appl. Phys. Lett. **112**, 091901 (2018).
[28] S. Kumar and H. P. Lee, Labyrinthine acoustic metastructures enabling broadband sound absorption and ventilation, Appl. Phys. Lett. **116**, 134103 (2020).